Unfiltering of the EarthCARE Broadband Radiometer (BBR) observations: the BM-RAD product

Almudena Velázquez Blázquez[1], Edward Baudrez[1], Nicolas Clerbaux[1], and Carlos Domenech[2]

[1]Royal Meteorological Institute of Belgium, Brussels
[2]GMV, Madrid, Spain

Correspondence: Almudena Velázquez Blázquez (almudena.velazquez@meteo.be)

Abstract. The methodology to determine the unfiltered solar and thermal radiances from the measured EarthCARE BBR shortwave (SW) and totalwave (TW) filtered radiances is presented. Within the EarthCARE ground processing, the correction for the effect of the BBR spectral responses, the unfiltering, is performed by the so-called BM-RAD processor which produces the level 2 BM-RAD product. The BM-RAD product refers to unfiltered broadband radiances that are derived from the BBR and the Multi-Spectral Imager (MSI) instruments onboard of the forthcoming EarthCARE satellite. The method is based on theoretical regressions between filtered and unfiltered radiances, as is done for the Clouds and the Earth's Radiant Energy System (CERES) and the Geostationary Earth Radiation Budget (GERB) instruments. The regressions are derived from a large geophysical database of spectral radiance curves simulated using radiative transfer models. Based on the radiative transfer computations, the unfiltering error, i.e., the error introduced by the small spectral variations of the BBR instrument response, is expected to remain well below 0.5% in the shortwave (SW) and 0.1% in the longwave (LW), at 1 standard deviation. These excellent performances are permitted by the very simple optics used in the BBR instrument: a telescope with a single paraboloid mirror. End-to-end verification of the unfiltering algorithm has been performed by running the BM-RAD processor on modeled Level 1 BBR radiances obtained for three EarthCARE orbits simulated by an integrated forecasting and data assimilation system. The resulting unfiltered radiances are eventually compared to the solar and thermal radiances derived by radiative transfer simulations over the three EarthCARE orbits. In addition, this end-to-end verification has provided further evidence on the high accuracy of the unfiltered radiance process, with accuracies better than 0.5% for SW and better than 0.1% for LW.

1 Introduction

The Broadband Radiometer (BBR) on board of the future EarthCARE satellite (Illingworth et al., 2015; Wehr et al., 2023) will measure accurate SW (0.25 to 5 μm) and TW radiances (0.25 to 500 μm) at three fixed viewing angles (fore, nadir and aft) along the EarthCARE track. The very fine spatial resolution of the detector array, 700 m along-track and 600 m across-track, allow to integrate the 3-views over different spatial domains. The radiances measured by the BBR are filtered by the spectral response of the instrument, that combines the detector response and the telescope and SW filter throughputs. Being directly dependent on the instrument's design, these filtered radiances are of little interest for the science community. They must be converted into

25   (unfiltered) solar and thermal radiances, which are the radiances that would be measured by a perfect instrument $\phi(\lambda) = 1$ that would be able to perfectly separate the reflected solar radiation from the Earth's emitted thermal radiation. In the EarthCARE ground processing, this unfiltering process is performed by the BM-RAD processor. In a later stage, the (unfiltered) radiances are converted into hemispheric fluxes, in a second BBR processor called BMA-FLX (Velázquez-Blázquez et al., 2023).

The BBR instrument is described in Proulx et al. (2010); Wallace et al. (2009); A.Helière (2017). It is composed of three
30   telescopes: a fore view at $\pm$ 55° forward, a nadir view at $\pm$ 0°, and an aft view at $\pm$ 55° backward. Any scene located under the satellite track is therefore observed from three directions almost at the same time (about 2 minutes between the fore and aft views). Each telescope uses an array of 30 microbolometer detectors, allowing an across-track swath of $\sim$ 17 km for the nadir view and $\sim$28 km for the two oblique views. The detectors' measurements will be averaged over different spatial domains, namely, *standard*, *small*, and *full*, which are defined by the L1 B-NOM product in the BBR grid (Spilling and Wright, 2020)
35   with an along-track sampling of 1 km. In addition, an additional configurable domain, the *Assessment Domain (AD)*, is defined on the Joint Standard Grid (JSG) for the radiative closure assessment of the EarthCARE mission (Barker et al., 2022). The main inputs to the BM-RAD processor are the level 1 B-NOM product that gives the filtered SW/LW radiances over the standard/small/full domains, the level 1 B-SNG product that gives the filtered SW/TW radiances at detector level, the MSI cloud mask and cloud phase product from M-CLD (Hünerbein et al., 2022), the Joint Standard Grid (X-JSG) and ancillary
40   meteorological data (X-MET) (Eisinger et al., 2023).

The paper is structured as follows. Section 2 presents the spectral response curves of the BBR instrument and introduces the unfiltering problem. Section 3 provides an overview of two large data bases of radiative transfer computations that are used to design and parameterize the unfiltering algorithm. Section 4 describes the unfiltering algorithm implemented in the BM-RAD processor. The performances of the algorithm are discussed in Section 5. An end-to-end verification of the algorithm and its
45   implementation in BM-RAD is then presented in Section 6 in which the processor is run on the three test scenes of 6200 km each. Final discussion is provided in Section 7.

2   BBR spectral responses and unfiltering problem statement

It is not possible to manufacture a broadband radiometer that has perfectly equal sensitivity to the radiation at all wavelengths. The thermal detector elements show some spectral structure in their responses, the throughput of the optics of the instrument
50   also results in spectral variations (Clerbaux, 2008a). The signal provided by the instrument, L_{fil}, is a radiance filtered by the spectral response $\phi(\lambda)$ of the instrument:

$$L_{fil} = \int L(\lambda)\phi(\lambda)d\lambda, \tag{1}$$

where $L(\lambda)$ is the input spectral radiance. For the BBR, the spectral responses of the total and shortwave channels are

Atmospheric
Measurement
Techniques
Discussions
Open Access
EGU

$$\phi_{tot}(\lambda) \quad = \quad \phi_{det}(\lambda)\,\phi_{tele}(\lambda), \tag{2}$$

$$\phi_{sw}(\lambda) \quad = \quad \phi_{det}(\lambda)\,\phi_{tele}(\lambda)\,\phi_{quartz}(\lambda), \tag{3}$$

in which $\phi_{det}(\lambda)$ is the spectral response of the detectors, $\phi_{tele}(\lambda)$ is the spectral reflectance of the telescope mirror, and $\phi_{quartz}(\lambda)$ is the transmittance of the quartz filter used for the SW channel.

Contrary to the SW channel, it is difficult to manufacture efficient and stable filter to isolate the LW radiation. For this reason, the longwave radiance is obtained by subtracting the SW part in the TW measurement as for the CERES and the GERB instruments. A "synthetic" LW radiance L_{lw} and spectral response $\phi_{lw}(\lambda)$ are therefore defined as:

$$L_{lw} \quad = \quad L_{tot} - A\,L_{sw}, \tag{4}$$

$$\phi_{lw}(\lambda) \quad = \quad \phi_{tot}(\lambda) - A\,\phi_{SW}(\lambda), \tag{5}$$

in which the A factor is defined in such a way that the longwave radiance L_{lw} is equal to exactly zero when an idealized black body solar spectrum of 5800 K is observed.

$$A = \frac{\int L_{5800\mathrm{K}}(\lambda)\phi_{tot}(\lambda)\,d\lambda}{\int L_{5800\mathrm{K}}(\lambda)\phi_{sw}(\lambda)\,d\lambda}, \tag{6}$$

where $L_{5800\mathrm{K}}$ is the Planck's emission for a temperature of $T = 5800$ K. As shown in Eq. 6, the factor A is not dependent on the observed scene $L(\lambda)$, but only on the instrument's spectral responses $\phi_{tot}(\lambda)$ and $\phi_{sw}(\lambda)$. Fig. 5 shows the SW, TW and synthetic LW spectral responses of the BBR instrument for the nadir view of the BBR. The curves for the fore and aft telescopes present only marginal difference with the nadir telescope (not shown).

The filtered radiances (L_{sw}, L_{lw}) are dependent on the instrument characteristics such as the number of mirrors in the optics and type of coating of these mirrors, the type of detector and coating, the thickness of the quartz filter, etc. For this reason, the filtered measurements have limited scientific interest and they must be converted into unfiltered quantities:

$$L_{unfil,sol} \quad = \quad \int L_{sol}(\lambda)d\lambda, \tag{7}$$

$$L_{unfil,th} \quad = \quad \int L_{th}(\lambda)d\lambda, \tag{8}$$

where the distinction is not performed in terms of wavelength λ but in terms of type of radiation: $L_{sol}(\lambda)$ corresponding to reflection of incoming solar radiation and $L_{th}(\lambda)$ to thermal emission in the Earth-atmosphere system. This conversion, called *unfiltering*, requires an accurate characterization of the instrument spectral response, $\phi(\lambda)$, but also some assumptions about the spectral signature $L(\lambda)$ of the observed scene, and the estimation of the contaminations of the SW channel with thermal radiation and of LW channel with solar radiation. The ratio between the unfiltered and filtered radiances is called either the *unfiltering factor* or the *spectral correction factor*, and are expressed as:

$$\alpha_{sol} \quad = \quad \frac{L_{unfil,sol}}{L_{sw,sol}} = \frac{\int L_{sol}(\lambda)\,d\lambda}{\int L_{sol}(\lambda)\phi_{sw}(\lambda)\,d\lambda}, \tag{9}$$

$$\alpha_{th} \quad = \quad \frac{L_{unfil,th}}{L_{lw,th}} = \frac{\int L_{th}(\lambda)\,d\lambda}{\int L_{th}(\lambda)\phi_{lw}(\lambda)\,d\lambda}. \tag{10}$$
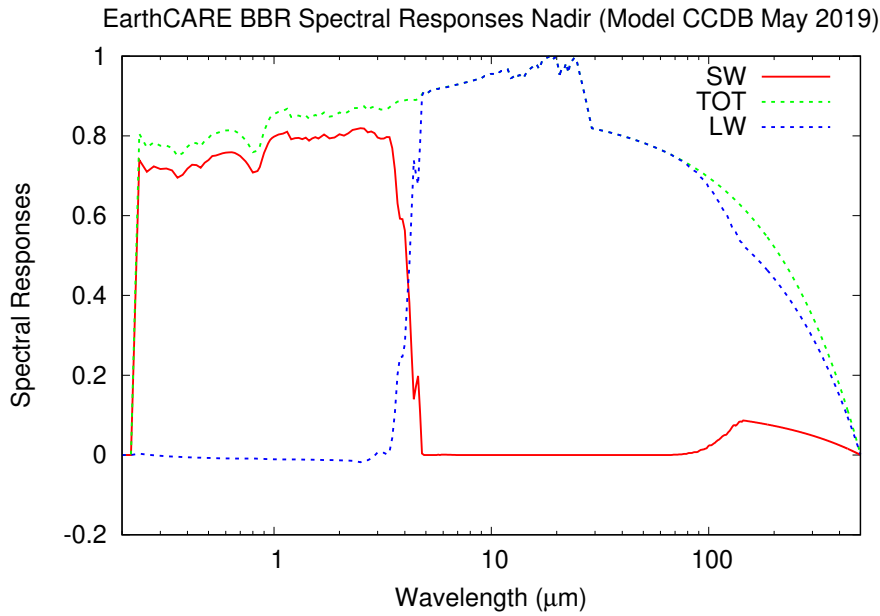
Figure 1. EarthCARE BBR spectral responses for the nadir view: shortwave channel $\phi_{sw}(\lambda)$ (red), total wave channel $\phi_{tot}(\lambda)$ (green) and synthetic longwave channel $\phi_{lw}(\lambda)$ (blue).

In this work, the unfiltering factors are estimated, off-line, from radiative transfer simulations for different scene types on which regressions are derived. These regressions are then used in the BM-RAD processor to infer the unfiltered radiances (L_{sol},L_{th}) from the filtered measurements (L_{sw}, L_{lw}). The contamination of both the SW channel by thermal radiation and of the LW channel by reflected solar radiation needs to be estimated prior to the actual unfiltering process. The mathematical forms of these contaminations are:

$$L_{sw,th} = \int \phi_{sw}(\lambda) L_{th}(\lambda) \, d\lambda, \tag{11}$$

$$L_{lw,sol} = \int \phi_{lw}(\lambda) L_{sol}(\lambda) \, d\lambda. \tag{12}$$

The thermal contamination in the SW channel, $L_{sw,th}$, accounts for the planetary thermal emission in the SW channel, below 5μm and also beyond 50μm due to the leak in the quartz filters in the far infrared region. The solar contamination in the LW channel, $L_{lw,sol}$, is generally negative as the synthetic LW spectral response is, very slightly, negative in shorter wavelengths (below 4μm). These small quantities should be subtracted from the measured shortwave L_{sw} and longwave L_{lw} radiances before the unfiltering process itself can be realized:

$$L_{sol} = \alpha_{sw} \, L_{sw,sol} = \alpha_{sw}(L_{sw} - L_{sw,th}), \tag{13}$$

$$L_{th} = \alpha_{lw} \, L_{lw,th} = \alpha_{lw}(L_{lw} - L_{lw,sol}). \tag{14}$$

So, the unfiltering process necessitates the estimation of four quantities: the two unfiltering factors (α_{sw}, α_{lw}) and the two contaminations ($L_{sw,th}$, $L_{lw,sol}$).

3 Radiative transfer simulations

100 The unfiltering coefficients and the contaminations are obtained theoretically from two large geophysical data bases: one of reflected solar radiances containing 5,544 simulations $L_{sol}(\lambda)$, and one of Earth's emitted thermal radiances containing 12,096 simulations $L_{th}(\lambda)$). These data bases are computed using the LibRadtran 1.4 (Mayer and Kylling, 2005) radiative transfer model as described in Velazquez et al. (2010). The simulations cover a wide range of physical conditions and for this purpose, the scene definition has been done using ancillary models and data, such as, surface reflectances from the Aster Spectral Library

105 data (Baldridge et al., 2009) and the Optical Properties of Aerosols and Clouds (OPAC) software (Hess et al., 1998) for the computation of the aerosol optical properties. Given that the Aster Spectral Library contains a large number of spectra, a k-means clustering of 12 clusters has been done for clear sky scenes. An averaging of the spectra has been done for those scenes with presence of aerosols. The simulations completely cover the illumination and observation geometries of EarthCARE .

Solar simulations have been done in the interval of 0.25 to 5μm, for 833 wavelenghts, with the following spectral resolution:

110 from 0.25 to 1.36 μm in steps of 0.002 μm, from 1.36 to 2.5 μm in steps of 0.005 μm and from 2.5 to 5 μm in steps of 0.05 μm. Thermal simulations have been done in the interval of 2.5 to 100 μm, for 762 wavelenghts, with the following spectral resolution: from 2.5 to 14 μm in steps of 0.05 μm, from 14.1 to 50 μm in steps of 0.1 μm and from 55 to 100 μm in steps of 0.5 μm. The limit at 100 μm for the simulations is due to the fact that ice and water cloud properties are defined up to this wavelength for both the Yang (Yang et al., 2000)(ice crystals) and Mie (water dropplets) parameterizations. As there is still

115 significant radiation beyond 100 μm, the longwave simulations $L_{th}(\lambda)$ have been extrapolated up to $\lambda = 500$ μm using the black body emission curve corresponding to the brightness temperature simulated at $\lambda = 100$ μm as in Clerbaux et al. (2008c).

The solar simulations $L_{sol}(\lambda)$ are performed for 9 Solar Zenith Angles (SZA, from 0 to 80 degrees in steps of 10 degrees), and the simulated radiance field is extracted at 18 Viewing Zenith Angles (VZA, $0°$ to $85°$ every $5°$), and 19 Relative Azimuth Angles (RAA, $0°$ to $180°$ every $10°$). The simulated radiances $L(\lambda)$ are convoluted with the SW, TW and LW spectral responses

120 $\phi(\lambda)$ of the BBR for each of the views (fore, nadir, aft) to obtain the filtered radiances for each geometry. The unfiltered radiances are obtained with a perfect constant "filter" $\phi(\lambda) = 1$.

4 The BM-RAD algorithm

4.1 Flowcharts

In the level 1 B-NOM product, the SW and LW filtered radiances are provided over areas defined according to the instrument

125 grid (the BBR grid). These domains are the *standard*, *small* and *full* integration domains. The level 2 BM-RAD products are then provided at the same domains as the level 1 input. The processing flowchart is given in the left panel of Fig. 2. Firstly, the solar contamination in the LW channel and the thermal contamination in the SW channel are estimated and subtracted from

the filtered LW and SW filtered radiances, respectively. In this way purely thermal and solar radiances are obtained. Secondly, the unfiltering coefficients are estimated and applied to obtain the unfiltered thermal and solar radiances. The level 1 B-SNG

130   product provides measurements of the SW and TW radiation at detector level. The B-SNG file is the main input to compute the level 2 BM-RAD products over the *Assessment Domain* (AD) which is defined on the mission Joint Standard Grid (JSG). The flowchart is shown in the right panel of Fig. 2, which also shows the additional estimation of the synthetic LW radiance.

Two algorithms have been developed for the shortwave: the "stand-alone" unfiltering that relies only on the BBR observations, and the "MSI-based" unfiltering in which cloud mask and cloud phase information from the MSI are used as additional

135   information to improve the accuracy of the unfiltering. In the stand-alone algorithm the regression coefficients are dependent on the geometry and surface type while in the MSI-based they are also dependent on the cloud mask, cloud phase and snow information from X-MET. For the LW only a stand-alone algorithm is implemented, as the unfiltering performs well within the requirements.
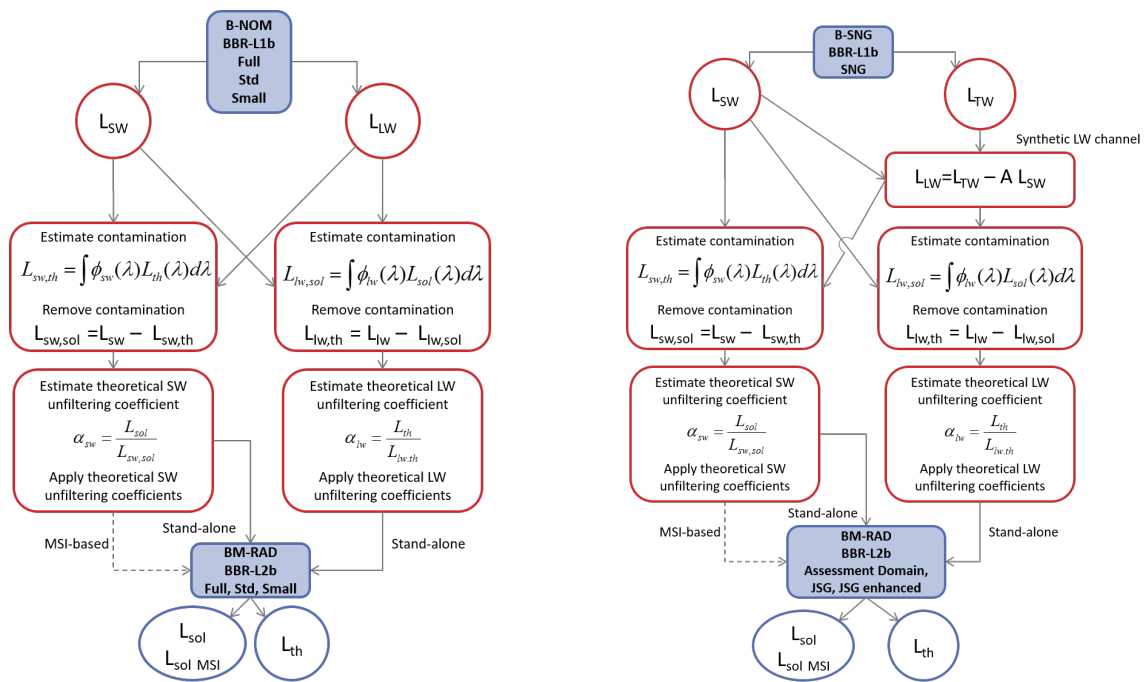

Figure 2. Unfiltering flowchart for the B-NOM product (left panel) and the B-SNG product (right panel).

4.2   Solar contamination in the LW channel

140   The Fig. 3 shows the scatter plots of the solar contamination in the LW channel, $L_{lw,sol}$, as a function of the solar radiances, $L_{sw,sol}$, for the four different surface types (rock, vegetation, ocean, and snow) and for clear and cloudy conditions. Each dot corresponds to one simulation in the libRadtran database. The figures illustrate two particular sun-target-satellite geometries, a sunglint case for the nadir view (SZA=0°, VZA=0°, RAA=0°) and a non- sunglint for the off-nadir views (SZA=30°, VZA=55°,

RAA=90°). The contamination of the synthetic LW channel with solar radiation is negative (as expected, as the synthetic LW
145 response is negative in the shortwave region) and shows a linear relationship with the intensity of the solar radiation. Therefore,
the contamination can be estimated as follows:

$$L_{lw,sol} = a \, L_{sw,sol}, \tag{15}$$

where the factor a is dependent on the geometry (SZA, VZA, RAA) but not on the surface type or the cloudiness. Flat ocean
scenes corresponding to sunglint situations have not been considered in the fit (i.e., scenes with sunglint angle lower than 10º
150 and wind speed is equal or lower to $1 \, ms^{-}1$) as with the 3 BBR views it will be possible to reduce the sunglint effects as the 3
telescopes will not subject to sunglint at the same time. The residual RMS error of the regression averaged for all the VZA in
the database is 0.034 $Wm^{-2}sr^{-1}$ which is acceptable for a typical signal in the LW channel (60 $Wm^{-2}sr^{-1}$). Higher errors
are expected for sunglint scenes, in which the error is estimated to be about 0.5 $Wm^{-2}sr^{-1}$ for a typical ocean clear sky LW
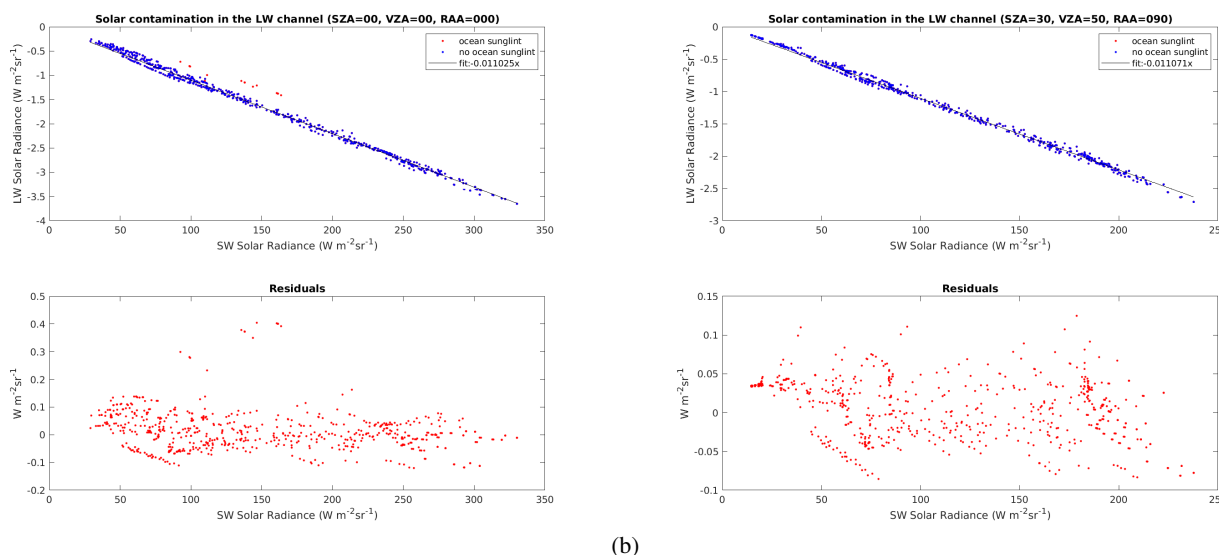radiance of 80 $Wm^{-2}sr^{-1}$.

(a)   (b)

Figure 3. Solar contamination in the LW channel. Represented here is the contamination for the nadir view of the BBR (a) for a sunglint
geometry (SZA=0°, VZA=0°, RAA=0°) and the off-nadir view (b) for a non-sunglint geometry (SZA=30°, VZA=55°, RAA=90°).

155 **4.3   Thermal contamination in the SW channel**

The Fig. 4 shows the scatter plots of the thermal contamination, $L_{sw,th}$, as a function of the thermal radiances, $L_{lw,th}$, for 4
different surface types (rock, vegetation, ocean, and snow) and for clear and cloudy conditions. This figure done for VZA=0° is
representative of the nadir view telescope of the BBR. The $L_{sw,th}$ contamination increases more than linearly with respect to
the scene thermal radiance, which is due to the shift of the Planck emission towards shorter wavelengths when the temperature

160 increases. A good fit is obtained with the following relationship:

$$L_{sw,th} = a + b\, L_{lw,th}^4, \tag{16}$$

in which the regression coefficients a and b are dependent on the VZA, but not on the surface or cloudiness types.
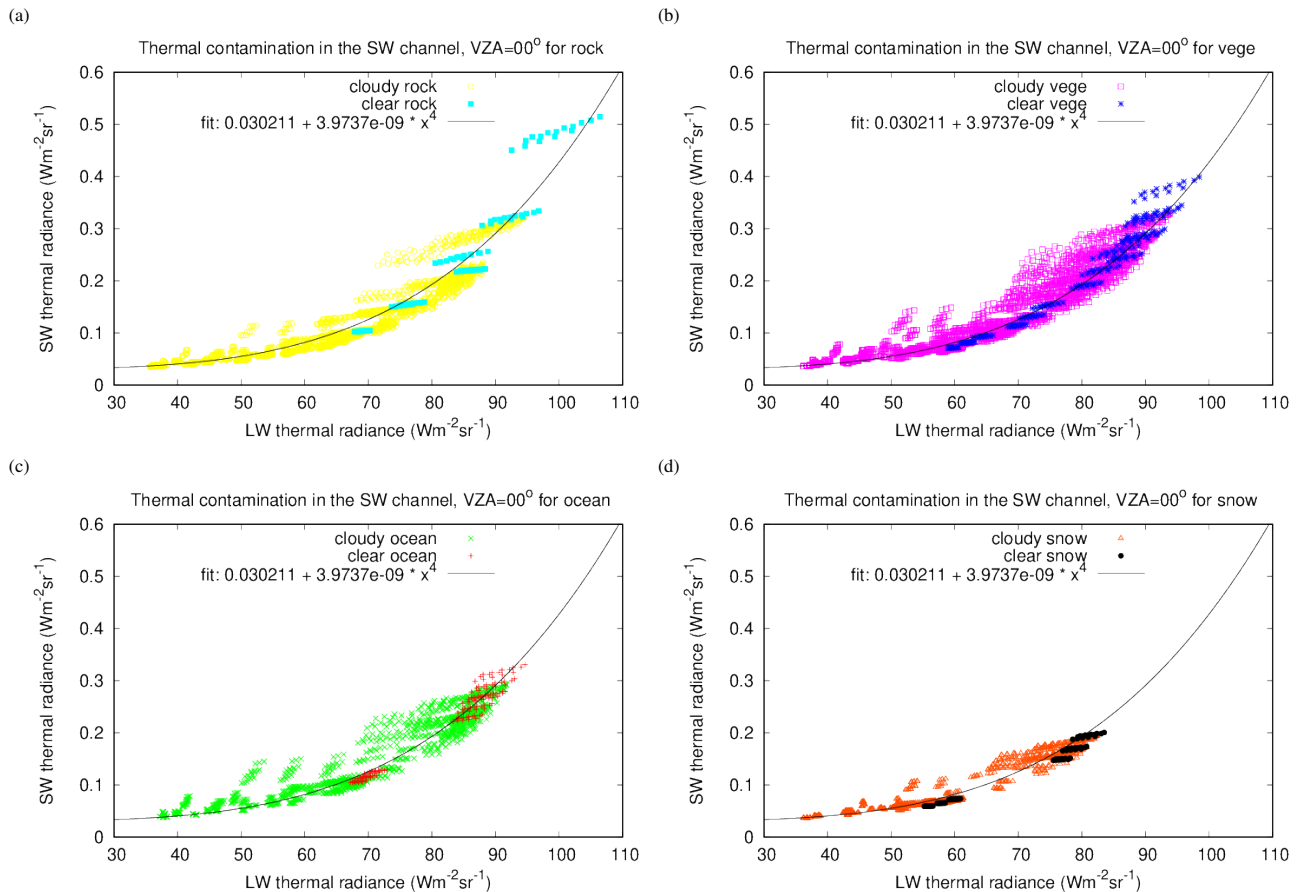

Figure 4. Thermal contamination in the SW channel for rock (a), vegetation (b), ocean (c), and snow (d) surfaces. Represented here is the contamination for the nadir view of the BBR. Very similar scatterplots, not shown, exist for the fore and aft views.

For the 12,096 scenes in the LW database, the contamination in the SW channel is lower than 0.6 $Wm^{-2}sr^{-1}$. The feather shape and variability in the LW thermal range comes from the wide range of water content in the water vapour profiles simulated

165 in the LW database. Higher errors in the estimation of the contamination are expected for very warm scenes like bright desert scenes and for scenes with a high water vapour content in warm atmospheres (e.g.,Tropical and Mid Latitude Summer). Ice phase high clouds (at 12 km in the simulations) also show higher errors than the rest of scenes. The residual RMS error on the estimation of the contamination, averaged over all the geometries in the database (VZA from 0° to 85° in steps of 5°), is 0.016 $Wm^{-2}sr^{-1}$, which is acceptable with respect to a typical signal in the SW channel of 100 $Wm^{-2}sr^{-1}$.

4.4 Stand-alone SW unfiltering

170

A first unfiltering algorithm that does not rely neither on the MSI radiances nor on cloud products has been developed. The motivation behind this is to enable the BBR data to be unfiltered even if the MSI observations are unavailable or if they become degraded with time. In addition, the stand-alone unfiltering algorithm may be useful to assess the problems introduced by the cloud parallax between the fore and aft views and the MSI nadir observation of the scene. An example of the distribution of

175 the unfiltering factors is given in figure 5 (top left panel) for a given geometry (SZA=30º, VZA=55º, RAA=90º) representative of the fore and aft views.

The other panels in figure 5 show the same data but separated according to the surface type (rock, vegetation, ocean, snow and soil). For most of the surface types, the best fit is obtained with the hyperbolic equation:

$$\alpha_{sw} = a + b/L_{sw,sol}, \tag{17}$$

180   which is identical to the $L_{sol} = b + a\,L_{sw,sol}$ relation used for the CERES (Loeb et al., 2001) and GERB (Clerbaux et al., 2008b) shortwave channels. The regression coefficients a and b are dependent on the surface type and on the viewing and solar geometries. The residual RMS error of the fit is provided in the different panels of Fig. 5. The typical RMS error of 0.004 $Wm^{-2}sr^{-1}$ corresponds to about 0.3% relative error on the unfiltering factor α_{sw}, thus also to 0.3% on the unfiltered radiance L_{sol}, and later also on the solar flux F_{sol}.
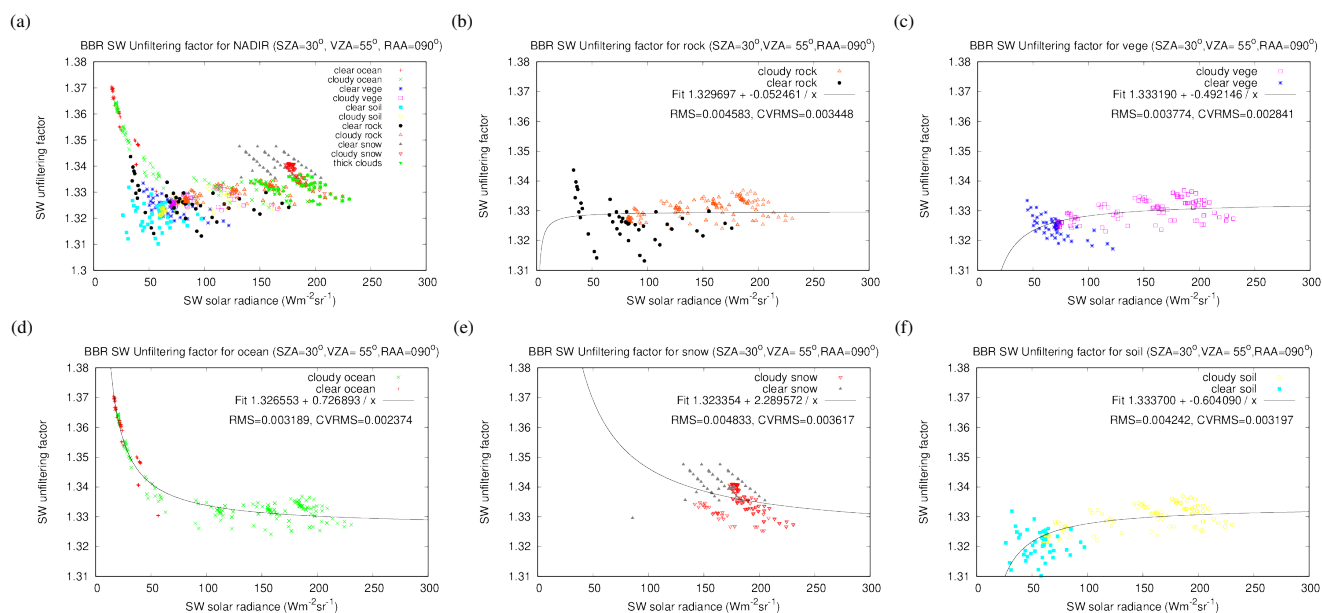

Figure 5. Stand-alone SW unfiltering for all scenes together (a) and then separated according to the surface type (rock (b), vegetation (c), ocean (d), snow (e) and soil(f)). These graphs are for the (SZA=30º, VZA=55º, RAA=90º) geometry, representative of the fore and aft views. Similar graphs exist for the nadir view (not shown).

4.5 MSI-based SW unfiltering

The objective of this scene dependent unfiltering is to further reduce the unfiltering error (evaluated at 0.3% at 1 standard deviation for the stand-alone, see previous section) using explicit information about the scene type within the BBR domains (*standard*, *small*, *full* or *Assessment Domain*). The study is similar to the stand-alone one, but the regressions (see equation 17) are in this case also dependent on the cloud mask (clear or cloudy condition) and the cloud phase (water droplets or ice crystals). Although the MSI-based algorithm provides slightly better results in the validation than the stand-alone, its applicability to the fore and aft views might be affected by cloud parallax effects, as the MSI provides a nadir view of the scene. The applicability of the MSI-based algorithm will be tested during the commissioning phase when real data will be available.

4.6 LW unfiltering

The LW channel unfiltering is illustrated in Fig. 6 which shows the scatterplots of the unfiltering factor α_{lw} versus the longwave thermal radiance $L_{th,lw}$, for the nadir view (left panel) and the VZA=55° views (right panel). The range of variability of the LW unfiltering factor for the BBR instrument is very reduced and much smaller than for the CERES and GERB instruments. A second degree polynomial fit in the scatterplots appears suitable to estimate the unfiltering coefficients:

$$\alpha_{lw} = a + b\, L_{lw,th} + c\, L_{lw,th}^2, \tag{18}$$

where the coefficients a, b, and c are dependent on the VZA. For clear sky warm scenes, the LW unfiltering factor presents enhanced variability due to variability in the spectral emissivity of the desert surfaces. Even though the performance of a single regression, with a RMS of about 0.1 %, is sufficient with respect to the scientific requirements of the mission, it was investigated if any improvement could be obtained using specific regressions for ocean, vegetation and desert surfaces. The improvement of using surface type dependent regressions is negligible and is therefore not further considered.
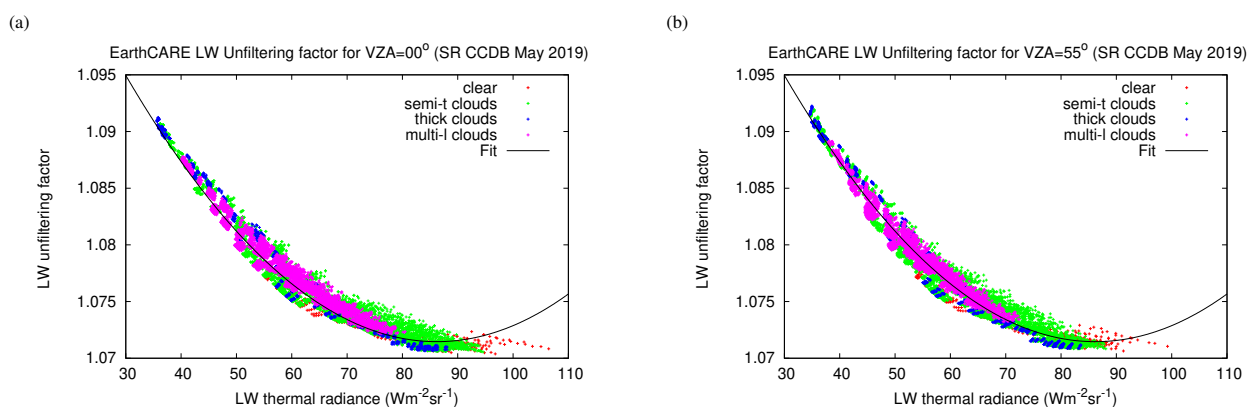

Figure 6. Scatter plot of unfiltering factors for the LW channel of the BBR, for VZA=0° (a) and 55° (b)

Type of scene	$N°$ of scenes SW	$<L_{sol}>$	RMS L_{sol}		$N°$ scenes LW	$<L_{th}>$	RMS L_{th}	
		$\mathrm{Wm^{-2}sr^{-1}}$	$\mathrm{Wm^{-2}sr^{-1}}$	(%)		$\mathrm{Wm^{-2}sr^{-1}}$	$\mathrm{Wm^{-2}sr^{-1}}$	(%)
thick high cloud	36	208.84	0.53	0.34	135	53.60	0.053	0.100
semi high cloud	120	117.34	0.30	0.34	702	61.07	0.058	0.095
semi high water cloud	60	117.77	0.30	0.34	702	61.07	0.059	0.097
semi high ice cloud	60	116.9	0.30	0.34	702	56.22	0.053	0.094
semi low cloud	60	112.53	0.29	0.34	702	72.19	0.063	0.088
thick low cloud	18	194.55	0.50	0.34	135	70.59	0.057	0.081
clear desert	43	89.74	0.29	0.42	90	78.96	0.079	0.100
clear ocean	56	39.4	0.10	0.35	135	77.21	0.075	0.098
clear snow	43	172.31	0.59	0.46	90	65.53	0.078	0.120
clear vege	43	75.5	0.21	0.36	225	74.85	0.079	0.107

Table 1. BBR unfiltering error analysis for 10 scene types (first column). For each scene type, the columns give: the number of libradtran simulations in the solar data base, the averaged solar radiance $<L_{sol}>$ and the RMS error on this radiance due to the subtraction of the thermal contamination and the error due to the unfiltering of the shortwave channel. The RMS error is expressed as an absolute value, in $\mathrm{Wm^{-2}sr^{-1}}$, and also as a relative error, in %. The last 4 columns provide the results for the unfiltering of the LW channel. Averaged values have been calculated over all the observation and illumination geometries, i.e, SZA [0:10:80], VZA [0:5:85] and RAA[0:10:180]

5 BM-RAD algorithm performance

An analysis of the unfiltering error is performed for 10 typical scene types covering the full extent in terms of SW and LW radiances. The error combines the one due to the estimation of the contamination and the error due to the estimation of the unfiltering factor. The results are summarized in Table 1 which provide values averaged over the full range of simulated SZA, VZA and RAA geometries. For the solar radiation, the relative error on the unfiltered radiances is $\approx 0.5\%$ in clear sky condition, and slightly lower in cloudy condition ($\approx 0.4\%$). For the thermal radiation, the relative error is well below 0.1 % for all of the scene types.

6 End-to-end verification of the algorithm using test scenes

In this section, data from the three EarthCARE test frames (Qu et al., 2022; Donovan et al., 2023) have been used to verify the performances of the BM-RAD processor. In general a close agreement is found between the unfiltered radiances calculated by the BM-RAD processor and the reference radiances (truth) obtained directly by broadband integration of the radiative transfer computations on the Global Environmental Multiscale Model (GEM) scenes. Table 2 details the results in terms of bias, RMS and standard deviation, all expressed in $\mathrm{Wm^{-2}sr^{-1}}$, and this for the 3 telescopes (fore, nadir, aft) and for the 3 test frames (Halifax, Baja, Hawaii). The table 2 summarises the performances of the stand-alone SW unfiltering, MSI-based SW unfiltering and stand-alone LW unfiltering.

From Table 2 it is clear that the MSI-based shortwave unfiltering does not perform significantly better than the stand-alone unfiltering, in both RMS and bias metrics. Another finding is that the unfiltering of the nadir view is in general more accurate

Scene	Halifax			Baja			Hawaii		
stand-alone SW	fore	nadir	aft	fore	nadir	aft	fore	nadir	aft
RMSE $(\mathrm{Wm^{-2}sr^{-1}})$	0.4864	0.3180	0.3787	1.0365	0.7305	0.8266	0.3729	0.4039	0.4159
stddev $(\mathrm{Wm^{-2}sr^{-1}})$	0.4253	0.2223	0.2996	0.8991	0.6773	0.7264	0.3289	0.3006	0.3806
bias $(\mathrm{Wm^{-2}sr^{-1}})$	-0.2361	-0.2273	-0.2317	0.5158	0.2737	0.3945	-0.1757	-0.2697	-0.1676
MSI-based SW	fore	nadir	aft	fore	nadir	aft	fore	nadir	aft
RMSE $(\mathrm{Wm^{-2}sr^{-1}})$	0.4616	0.3142	0.3817	1.0071	0.7926	0.9197	0.3995	0.3852	0.4030
stddev $(\mathrm{Wm^{-2}sr^{-1}})$	0.4014	0.2168	0.2869	0.9421	0.7494	0.8364	0.3652	0.066	0.3727
bias $(\mathrm{Wm^{-2}sr^{-1}})$	-0.2279	-0.2275	-0.2518	0.3557	0.258	0.3825	-0.1621	-0.2332	-0.1534
LW	fore	nadir	aft	fore	nadir	aft	fore	nadir	aft
RMSE $(\mathrm{Wm^{-2}sr^{-1}})$	0.1601	0.1052	0.1169	0.2387	0.2460	0.2210	0.3114	0.3432	0.3160
stddev $(\mathrm{Wm^{-2}sr^{-1}})$	0.15223	0.0903	0.1061	0.2368	0.2431	0.2191	0.3015	0.3323	0.3063
bias $(\mathrm{Wm^{-2}sr^{-1}})$	0.0498	0.0539	0.049	0.0306	0.0377	0.029	0.0776	0.0861	0.0777

Table 2. Statistics of the BBR unfiltering errors for the 3 test scenes (Halifax, Baja, Hawaii) and each of the 3 views of the BBR (fore, nadir, aft). The upper parts of the table provide the errors for the stand-alone and MSI-based unfiltering of the SW channel. The bottom part is for the (stand-alone) unfiltering of the longwave channel.

than the one of the fore and aft views (with, however, an exception for the stand-alone shortwave unfiltering for the Hawaii scene).

The Fig. 7 shows the unfiltering results along the frame for the three test scenes. The upper panels show the radiances (filtered, unfiltered and truth) along the track, and the lower panels show the differences between the BM-RAD unfiltered radiance and the truth. The lower panels also provide the mean difference (bias), the standard deviation and the RMS error.

7 Conclusions

In this paper, the algorithms used by the unfiltering processor (BM-RAD) for the BBR instrument onboard EarthCARE are described. The main output of BM-RAD are the unfiltered solar and thermal radiances for the three BBR views integrated over different spatial domains. These radiances are the main input for the BMA-FLX processor in which the three views are combined to estimate the hemispheric outgoing shortwave and longwave radiative fluxes.

Thanks to its design, the BBR instrument sensitivity shows limited spectral variability which is a pre-requisite for an accurate unfiltering process. The typical stand-alone unfiltering errors are expected to be approximately 0.5% for the shortwave channel and well below 0.1% for the longwave channel. These good results have been verified using the three EarthCARE test scenes (Halifax, Baja, Hawaii).

Scene information from the MSI radiances (from M-RGR product), MSI cloud retrievals (from M-CLD processor), or snow products (from X-MET product) are useful to further reduce the unfiltering error. So, in addition to the stand-alone unfiltered
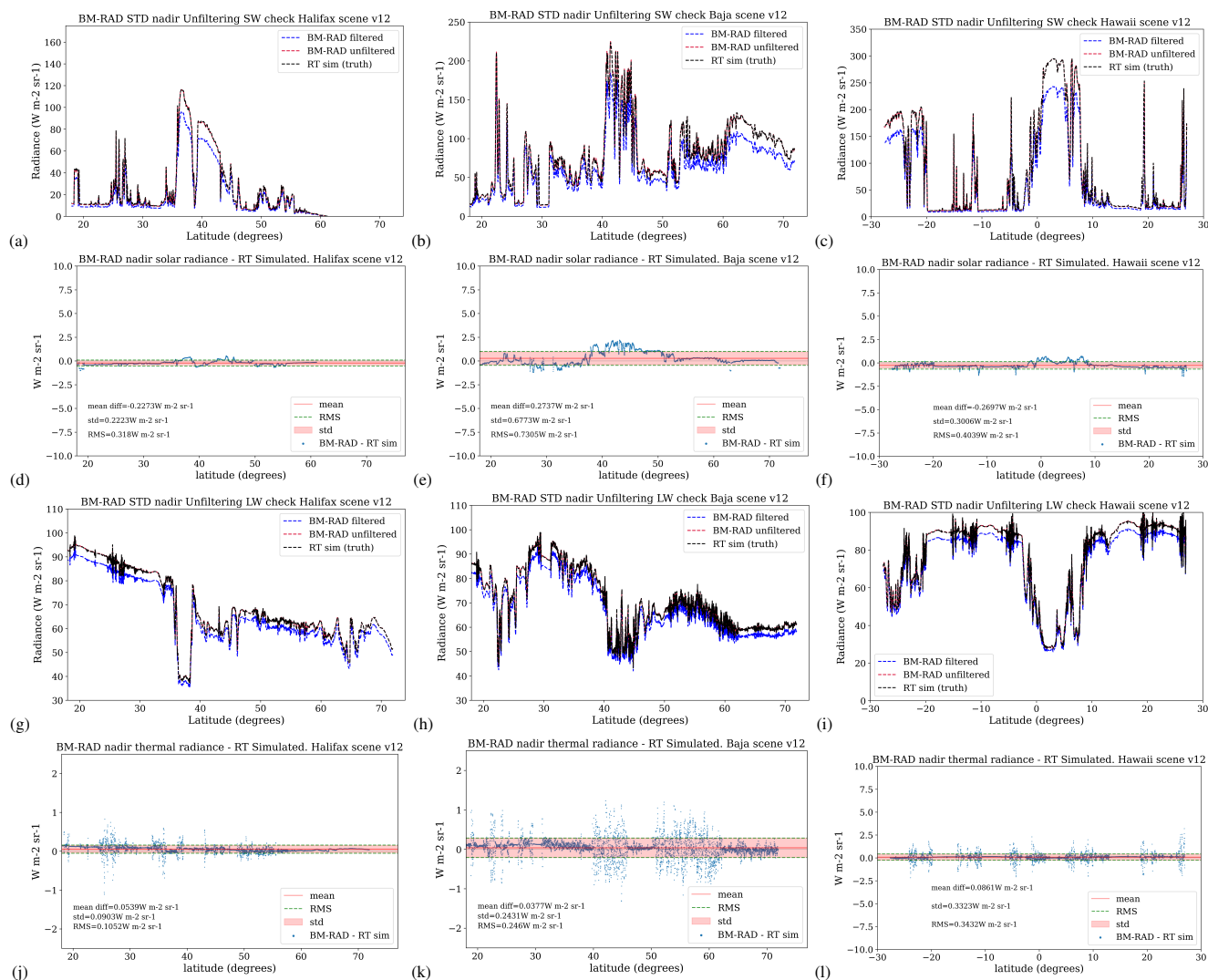
Figure 7. Filtered and unfiltered radiances versus the radiative transfer simulations ("RT truth") across the 3 test scenes of Halifax (a,g), Baja (b,h) and Hawaii (c,i). The (a,b,c) panels show the shortwave radiances along the satellite track (and goes to zero in night time condition). The (g,h,i) panels show the corresponding results for the longwave radiation. The difference between the BM-RAD unfiltered solar radiance and the reference value is shown in (d,e,f) and the corresponding differences for the thermal radiances are shown in (j,k,l). The graphs shown here correspond to the nadir view. Similar results are obtained for the off-nadir views (not shown).

radiances, the BM-RAD product also contains the MSI-based unfiltered radiance for the shortwave radiation (the improvement for the longwave radiance was considered negligible and therefore not included in the product). However, the MSI-based unfiltering of the fore and aft views might suffer from the parallax effect as the MSI provides only nadir observations. Therefore, 240 a comprehensive evaluation of the MSI-based unfiltering is foreseen to be carried out during the commissioning phase, when the

BM-RAD processor can be applied on real BBR and MSI observations. In the meantime, the stand-alone unfiltered radiances should be used.

Data availability. The EarthCARE demonstration products from the simulated scenes, including B-NOM and B-SNG L1 data and the BM-RAD L2 products discussed in this paper are available from https://doi.org/10.5281/zenodo.7728948 (van Zadelhoff et al., 2023)

245 *Author contributions.* The manuscript was prepared by AVB, EB, NC and CD. The BM-RAD software was developed by AV, EB and NC

Competing interests. The authors declare that they have no conflict of interest

References

250 J. P. d. C. M. T. A. A.Helière, K. Wallace. EarthCARE Instruments Description 1.0. EC-TN-ESA-SYS-0891. Technical report, ESA, 2017.

A. Baldridge, S. Hook, C. Grove, and G. Rivera. The ASTER Spectral Library Version 2.0. *RSE*, 113:711–715, 2009.

H. W. Barker, J. N. S. Cole, Z. Qu, N. Villefranque, and M. Shephard. Earthcare's continuous radiative closure assessment: Summary and application to data from a synthetic observing system. *Atmospheric Measurement Techniques*, to be submitted, 2022.

N. Clerbaux. *Processing of Geostationary Satellite Observations for Earth Radiation Budget Studies*. PhD thesis, Vrije Universiteit Brussel
255 (VUB), 2008a. Available at https://gerb.oma.be/.

N. Clerbaux, S. Dewitte, D. Bertrand, C.and Caprion, B. De Paepe, and A. Ipe. Unfiltering of the Geostationary Earth Radiation Budget (GERB) Data. Part I: Shortwave Radiation. *Journal of Atmospheric and Oceanic Technology*, 25:1087–1105, 2008b.

N. Clerbaux, S. Dewitte, D. Bertrand, C.and Caprion, B. De Paepe, and A. Ipe. Unfiltering of the Geostationary Earth Radiation Budget (GERB) Data. Part II: Longwave Radiation. *Journal of Atmospheric and Oceanic Technology*, 25:1106–1117, 2008c.

260 D. P. Donovan, P. Kollias, A. Velázquez Blázquez, and G.-J. van Zadelhoff. The generation of earthcare l1 test data sets using atmospheric model data sets. *EGUsphere*, 2023:1–54, 2023. https://doi.org/10.5194/egusphere-2023-384. URL https://egusphere.copernicus.org/preprints/2023/egusphere-2023-384/.

M. Eisinger, T. Wehr, T. Kubota, D. Bernaerts, and K. Wallace. The EarthCARE production model and auxiliary products. *Atmospheric Measurement Techniques*, to be submitted, 2023.

265 M. Hess, P. Koepke, and I. Schult. Optical properties of aerosols and clouds: the software package opac. *Bulletin of the american Meteorological Society*, 79(5):831–844, 1998.

A. Hünerbein, S. Bley, S. Horn, H. Deneke, and A. Walther. Cloud mask algorithm from the earthcare multi-spectral imager: the m-cm products. *EGUsphere*, 2022:1–23, 2022. https://doi.org/10.5194/egusphere-2022-1240. URL https://egusphere.copernicus.org/preprints/2022/egusphere-2022-1240/.

270 A. J. Illingworth, H. W. Barker, A. Beljaars, M. Ceccaldi, H. Chepfer, N. Clerbaux, J. Cole, J. Delanoë, C. Domenech, D. P. Donovan, S. Fukuda, M. Hirakata, R. J. Hogan, A. Huenerbein, P. Kollias, T. Kubota, T. Nakajima, T. Y. Nakajima, T. Nishizawa, Y. Ohno, H. Okamoto, R. Oki, K. Sato, M. Satoh, M. W. Shephard, A. Velázquez-Blázquez, U. Wandinger, T. Wehr, and G.-J. van Zadelhoff. The EarthCARE Satellite: The Next Step Forward in Global Measurements of Clouds, Aerosols, Precipitation, and Radiation. *Bulletin of the American Meteorological Society*, 96(8):1311–1332, 8 2015. ISSN 0003-0007. https://doi.org/10.1175/BAMS-D-12-00227.1. URL
275 http://journals.ametsoc.org/doi/abs/10.1175/BAMS-D-12-00227.1.

N. Loeb, K. Priestley, D. Kratz, E. Geier, R. Green, B. Wielicki, P. Hinton, and S. Nolan. Determination of Unfiltered Radiances from the Clouds and the Earth's Radiant Energy System instrument. *JAM*, 40:822–835, 2001.

B. Mayer and A. Kylling. Technical note: The libRadtran software package for radiative transfer calculations - description and examples of use. *Atmos. Chem. Phys.*, 5:1855–1877, 2005.

280 C. Proulx, M. Allard, T. Pope, B. Tremblay, F. Williamson, J. Delderfield, and D. Parker. EarthCARE BBR detectors performance characterization. In R. Meynart, S. P. Neeck, and H. Shimoda, editors, *Sensors, Systems, and Next-Generation Satellites XIV*, volume 7826, pages 498 – 508. International Society for Optics and Photonics, SPIE, 2010. https://doi.org/10.1117/12.868518. URL https://doi.org/10.1117/12.868518.

Z. Qu, D. P. Donovan, H. W. Barker, J. N. S. Cole, M. Shephard, and H. V. Numerical model generation of test frames for pre-launch
  studies of EarthCARE's retrieval algorithms and data management system. *Atmospheric Measurement Techniques Discussions*, 2022,
  2022. https://doi.org/https://doi.org/10.5194/amt-2022-300. URL https://amt.copernicus.org/preprints/amt-2022-300/.

D. Spilling and N. Wright. ECGP Algorithm Theoretical Baseline Document. EC-TN-SEA-BBR-0005. Technical report, October 2020.

G.-J. van Zadelhoff, H. W. Barker, E. Baudrez, S. Bley, N. Clerbaux, J. N. S. Cole, J. de Kloe, N. Docter, C. Domenech, D. P. Donovan,
  J.-L. Dufresne, M. Eisinger, J. Fischer, R. García-Marañón, M. Haarig, R. J. Hogan, A. Hünerbein, P. Kollias, R. Koopman, N. Madenach,
  S. L. Mason, R. Preusker, B. Puigdomènech Treserras, Z. Qu, M. Ruiz-Saldaña, M. Shephard, A. Velázquez-Blázquez, N. Villefranque,
  U. Wandinger, P. Wang, and T. Wehr. EarthCARE level-2 demonstration products from simulated scenes, Mar. 2023. URL https://doi.org/
  10.5281/zenodo.7728948.

A. Velazquez, N. Clerbaux, H. Brindley, S. Dewitte, A. Ipe, and J. Russel. Global spectral Databases of simulated solar and thermal radiance
  fields at the TOA. Technical Description SITS, deliverable D3, RMIB, 2010.

A. Velázquez-Blázquez, E. Baudrez, N. Clerbaux, C. Domenech, R. G. Marañón, and N. Madenach. Towards instantaneous top-of-
  atmosphere fluxes from EarthCARE: the BMA-FLX product. *Atmospheric Measurement Techniques*, to be submitted, 2023.

K. Wallace, N. Wright, D. Spilling, K. Ward, and M. Caldwell. The broadband radiometer on the earthcare spacecraft. *Proc. SPIE, Infrared
  Spaceborne Remote Sensing and Instrumentation XVII, 2 September 2009*, 7453, 08 2009. https://doi.org/10.1117/12.825837.

T. Wehr, T. Kubota, G. Tzeremes, K. Wallace, H. Nakatsuka, Y. Ohno, R. Koopman, S. Rusli, M. Kikuchi, M. Eisinger, T. Tanaka,
  M. Taga, P. Deghaye, E. Tomita, and D. Bernaerts. The earthcare mission – science and system overview. *EGUsphere*, 2023:1–47,
  2023. https://doi.org/10.5194/egusphere-2022-1476. URL https://egusphere.copernicus.org/preprints/2023/egusphere-2022-1476/.

P. Yang, K. Liou, K. Wyser, and D. Mitchell. Parameterization of the scattering and absorption properties of individual ice crystals. *J.
  Geophys. Res.*, D4:4699–4718, 2000.